Biophysical Journal Volume 102 May 2012 2241–2250

Mapping Three-Dimensional Stress and Strain Fields within a Soft Hydrogel Using a Fluorescence Microscope

Matthew S. Hall,[†△] Rong Long,[†‡△] Chung-Yuen Hui,[‡*] and Mingming Wu[†*]

[†]Department of Biological and Environmental Engineering and [‡]Field of Theoretical and Applied Mechanics, Cornell University, Ithaca, New York

ABSTRACT Three-dimensional cell culture is becoming mainstream as it is recognized that many animal cell types require the biophysical and biochemical cues within the extracellular matrices to perform truly physiologically realistic functions. However, tools for characterizing cellular mechanical environment are largely limited to cell culture plated on a two-dimensional substrate. We present a three-dimensional traction microscopy that is capable of mapping three-dimensional stress and strain within a soft and transparent extracellular matrix using a fluorescence microscope and a simple forward data analysis algorithm. We validated this technique by mapping the strain and stress field within the bulk of a thin polyacrylamide gel layer indented by a millimeter-size glass ball, together with a finite-element analysis. The experimentally measured stress and strain fields are in excellent agreements with results of the finite-element simulation. The unique contributions of the presented three-dimensional traction microscopy technique are: 1), the use of a fluorescence microscope in contrast with the confocal microscope that is required for the current three-dimensional traction microscopes in the literature; 2), the determination of the pressure field of an incompressible gel from strains; and 3), the simple forward-data-analysis algorithm. Future application of this technique for mapping animal cell traction in three-dimensional nonlinear biological gels is discussed.

INTRODUCTION

Biomechanical cues from the extracellular matrix (ECM), such as adhesion and compliance, play important roles in functions of most animal cell types (1,2). When plated on a two-dimensional substrate, cells grow (3), differentiate (4), and migrate (5–7) differently based on the substrate compliance and the adhesiveness. Substrate compliance influences adhesion structures and dynamics (6), cytoskeleton assembly, and cell spreading (8,9). A notable example is that human mesenchymal stem cells are found to differentiate into cells that exhibit neurogenic, myogenic, and osteogenic phenotypes when plated on polyacrylamide gel substrates with soft, stiffer, and very stiff matrices, respectively (4).

In vivo, most animal cells reside in a three-dimensional ECM, and require the biophysical and biochemical cues from the ECM to perform truly physiologically relevant cellular functions (10–13). Indeed, cells are found to exhibit smaller focal adhesion complexes, downgrading integrin expressions in three-dimensional ECM in comparison to their counterparts in two-dimensional ECM (14). As a result, an increasing number of in-vitro models culture cells within the bulk of three-dimensional hydrogels, instead of the traditional two-dimensional substrates (10,11,15,16). However, tools available as of this writing for characterizing stress and strain fields within a soft biomaterial, such as traction microscopy, are largely limited to two-dimensional substrates (17–19). There is a need for developing tools for quantifying three-dimensional strain and stress fields within a three-dimensional ECM.

Three-dimensional traction microscopy, designed to map the stress and strain field in three-dimensional ECM, is still in its infant stage (20–22). This is due in part to the requirement of a confocal microscope that is often not available in the labs of individual investigators, and in part to the complex data analysis algorithm required. Maskarinec et al. (20) and Franck et al. (23) measured the three-dimensional displacement, strain, and stress field within a thin layer of polyacrylamide gel deformed by a single fibroblast cell cultured on the gel surface. They used confocal microscopy to image the micrometer size fluorescent beads embedded in the gel and determined the displacement fields using a digital-volume correlation method (24). Concurrently, Hur et al. (21) developed a different method to measure the three-dimensional stress and strain field within a polyacrylamide gel deformed by a single endothelial cell, cultured on the gel surface. They also used confocal microscopy to image fluorescent beads embedded in the gel. Bead positions were determined by finding the maximum intensity of the bright spots, and displacements were determined using the nearest-neighbor and a bead-pattern recognition algorithm. The bead displacements were then used as boundary conditions to solve the three-dimensional governing equations of linear elasticity through finite-element analysis. Both of these works clearly demonstrated that cells exert three-dimensional tractions even when cultured on two-dimensional substrates.

More recently, Legant et al. (22) quantified cellular tractions of a single cell cultured within a synthetic elastic hydrogel. They used embedded fluorescent beads in

Submitted January 7, 2012, and accepted for publication April 6, 2012.

△Matthew S. Hall and Rong Long contributed equally to this work.

*Correspondence: mw272@cornell.edu or ch45@cornell.edu

Editor: Andrew McCulloch.

0006-3495/12/05/2241/10 $2.00

doi: 10.1016/j.bpj.2012.04.014

conjunction with a confocal microscope for measuring bead displacements due to cellular tractions. The cell surface was reconstructed from confocal microscopy and was discretized into small elements. Finite-element calculations were then performed to obtain the discretized Green's functions on these surface elements. An ill-posed inverse problem was then solved using an optimization method to determine the cell tractions from the bead displacements. This method provided a high-spatial-resolution three-dimensional traction field at the cell surface, but required that the gel be linearly elastic, isotropic, and homogeneous—an inherent limitation when using the superposition of Green's functions. In addition, this technique needs a large volume of image-data acquisition and complex data processing.

Motivated by the need to map the stress and strain field around a single cell for studies of cell-ECM interactions, we developed a three-dimensional traction microscopy that allows for the mapping of the strain and stress field within a soft and transparent hydrogel using a fluorescence microscope and a simple-to-implement forward data analysis algorithm. This technique takes advantage of a recently developed three-dimensional defocused particle-tracking method (25) for bead-displacement measurements and a moving least-square interpolation method (MLSIM) for the computation of the strain field from the bead displacements (26). As a result, it allows for the use of a fluorescence instead of confocal microscope, and improves the temporal resolution of the current three-dimensional traction microscope from a few minutes to a few seconds. Furthermore, this technique is not limited to the linear elastic gel and can be readily modified to study cellular traction within biological gels (i.e., often display nonlinear elasticity (27)) such as collagen.

MATERIALS AND METHODS

Binding a polyacrylamide gel to an activated cover slide

Glass coverslips of two different sizes were used in this procedure. One side of a smaller glass coverslip (No. 1, 45 × 50 mm; ThermoScientific, Waltham, MA) was treated with the product Rain-X (Houston, TX) to make it hydrophobic. The surface of a larger glass coverslip (No. 1, 48 × 65 mm; Thermo Scientific, Waltham, MA) was activated to covalently bond to a polyacrylamide gel sheet using methods adapted from the protocol of Reinhart-King et al. (28). First, a cotton swab was used to evenly coat the surface with 0.1 N NaOH and the coverslip was air-dried. Second, a Pasteur pipette was used to coat the surface with 60 μL of 3-aminopropyltrimethoxysilane (APTMS; Aldrich, St. Louis, MO). After incubating 5 min, the coverslip was washed with distilled water and air-dried. Third, the coverslip was coated with 2 mL of 0.5% glutaraldehyde (70%; Aldrich) in phosphate-buffered saline and incubated for 30 min. Last, the coverslip was washed in distilled water and air-dried to complete the surface activation.

A polyacrylamide solution with a final concentration of 3% acrylamide (40% w/v; Bio-Rad, Hercules, CA), 0.1% *n*, *n*-methylene-bis-acrylamide (2% w/v BIS; Bio-Rad), 300 mM HEPES (EMD Chemicals, Gibbstown, NJ), 0.05% Tetramethyl ethylenediamine (TEMED; Sigma, St. Louis, MO), and 0.83-μm green fluorescent microspheres (Cat. No. G830; ThermoScientific) was prepared. The solution was adjusted to a pH of 6 with hydrochloric acid and then degassed. Molecular biology grade ethyl alcohol was added to achieve a final concentration of 7%. Ammonium persulfate (Aldrich) was added to achieve a final concentration of 0.05% w/v to initiate polymerization. The polyacrylamide solution was pipetted onto the hydrophobic side of the smaller coverslip. The activated side of the larger coverslip was lowered into contact with the polyacrylamide solution until the solution covered the entire area of the smaller coverslip. The polyacrylamide layer and smaller coverslip were suspended upside-down from the larger coverslip to polymerize for 2 h in a 100% humidity environment. The smaller coverslip was removed and the polyacrylamide gels were immersed in distilled water for at least one day to ensure complete hydration before use.

Indentation method

We used the weight of a millimeter-scale glass sphere to deform a thin polyacrylamide gel layer (see Fig. 1). This method, known as the indentation method, was pioneered by Frey et al. (18) for determining the Young's modulus of soft gel. A spherical glass ball with specific density of 2.5 g/mL and diameter of 1.17 mm was used. The indentation force, equal to the weight minus the buoyancy force of the glass sphere, was 12.4 μN. For each indentation experiment, a pipette was used to place the glass sphere on the surface of the polyacrylamide gel covered by water submerging both the gel and the sphere. The sphere was then brought to the center of the image using the *x*-*y* translation stage of the microscope (model No. IX51; Olympus) and the bright-field microscopy. The microscope was then switched to epi-fluorescent mode. An image of the fluorescent beads embedded within the gel was captured with the 20× objective (NA 0.4; Olympus). A pipette was then used to push the glass indenter off the gel with a gentle jet of water without disturbing the gel or microscope stage. The gel returned to its un-deformed state, and a second image of the fluorescent beads was captured with the 20× objective without adjusting the stage location. We defined the center of the coordinate (0,0,0) to be at the contact point of the un-deformed sphere-gel interface (see Fig. 1) and used it as a reference point for all data-taking. The gel thickness was determined by measuring the locations of the highest and lowest fluorescent beads in the gel using the manual *z*-translation stage (29), which was $h = 134 \pm 2.3$ μm. This procedure was repeated at 10 different locations on the surface of the gel using the same sphere.

A three-dimensional defocused particle tracking method

A defocused particle-tracking method was used to measure the three-dimensional positions of the fluorescent beads embedded within the gel (25) (see Fig. 1). The basic idea behind the defocused particle-tracking method is shown in Fig. 2 *A*. When a point light source is positioned at the focal plane, the light converges to a point in the image plane. When the point light source

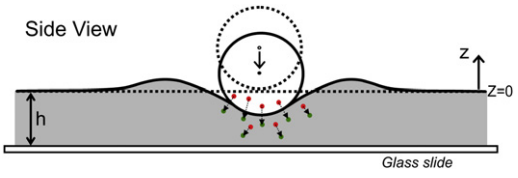

FIGURE 1 Microsphere indentation method. Schematics of a microsphere indenting on a thin polyacrylamide gel substrate. The contact point of the sphere with the un-deformed gel is defined as the origin or (0,0,0) coordinates of the system with *z* axis being in the vertical direction. Fluorescent beads embedded in the gel are displaced from their original positions (*red dots*) to their final positions (*green dots*) upon the indentation of the microsphere.

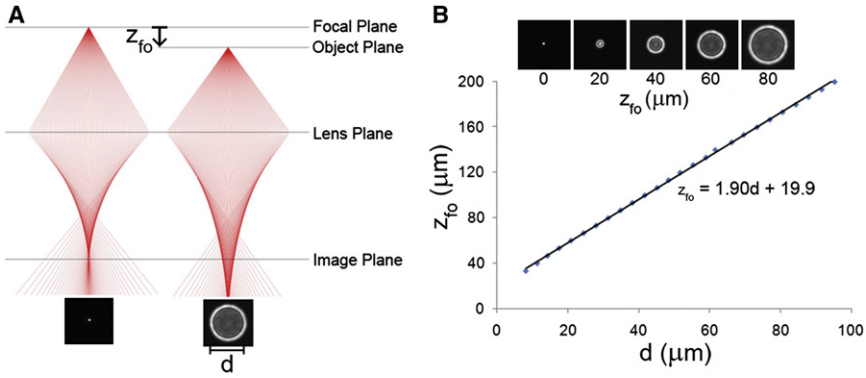

FIGURE 2 Three-dimensional defocused particle-tracking method. (*A*) A ray-tracing diagram of light traveling through a spherical lens. A point source of light in the focal plane emits rays that are bent by the lens and converge to a point at the image plane (*left side*). If the point source is displaced a distance z_{fo} from the focal plane, its rays do not converge and they produce a defocused ring on the image plane with diameter d (*right side*) due to spherical aberration. Representative images of a point source under each condition are inserted (*bottom*). (*B*) Experimentally derived calibration curve of fluorescent bead z_{fo} versus defocused-ring diameter d. Images of defocused rings at different z_{fo} are inserted (*top*).

is a distance z_{fo} from the focal plane, the light converges into a circular ring of diameter d in the image plane due to spherical aberration in the microscope objective lens (Fig. 2 *A*). In our microscope system, the defocused ring is only observed when the point light source is positioned between the focal plane and the lens plane. The ring image can then be used to compute the (x,y,z) coordinates of the point light source.

To compute the z position of the fluorescent bead using the ring diameter, we carried out a calibration for our optical system. We measured the distance from the focal plane, z_{fo}, as a function of the ring diameter d. Fig. 2 *B* shows that z_{fo} was linearly related to d over the z_{fo} range of (30–200 μm) for the 20× objective lens (Fig. 2 *B*). To obtain this calibration curve, we first brought a 0.83-μm green fluorescent microsphere (Cat. No. G830; ThermoScientific) into focus. The objective lens was then brought closer to the fluorescent bead in the z direction in 5-μm increments and an image was taken at each increment. The diameter of the ring in each image was measured using the image analysis software detailed below. It should be noted that the lens was displaced along the z direction during the calibration procedure, whereas the experimental measurements were made relative to the focal plane. In our system, displacement of the lens is not equal to displacement of the focal plane because of refractive index mismatches at the air-glass and glass-water interfaces.

To account for this difference, a calibration was performed using a known spacing (an equivalent of a z-ruler) submerged in water (29). The calibration showed that the displacement of the focal plane was 1.31 times the displacement of the lens. The experimentally derived optical correction factor 1.31 is comparable to the correction factor computed from Gaussian optics of 1.33 where the objective lens is treated as a thin lens, the cover slide is negligibly thin, and the paraxial approximation applies. A separate calibration experiment was performed to ensure the same z_{fo}-versus-d relationship applies to fluorescent beads at all locations throughout the gel. The slope of the z_{fo}-versus-d linear fit was found to vary by <2% between beads at the top and bottom of the gel.

Image analysis

The (x,y,z) coordinates of the fluorescent beads were obtained from the ring image shown in Fig. 3 *A* using an in-house customized MATLAB program (MATLAB, The MathWorks, Natick, MA). For each ring, the user first provided an approximation for the center and diameter of the ring through a graphical user interface by clicking at three points on the circumference of the ring. A search algorithm was then used to find the exact center and diameter of the ring with spatial resolution of one pixel. The (x,y) coordinates of the fluorescent bead were determined using the center position of the ring, and the z coordinate of the bead was determined using the ring diameter and the calibration curve shown in Fig. 2 *B*.

The fluorescent bead displacements were obtained by tracking the bead positions of the two images taken before and after the gel deformation (Fig. 3 *A*). To increase the spatial resolution of the bead displacements, results from 10 separate indentations with the same spherical indenter were combined into one dataset. It should be noted that it is important that the contact point between the indenter and the un-deformed gel be

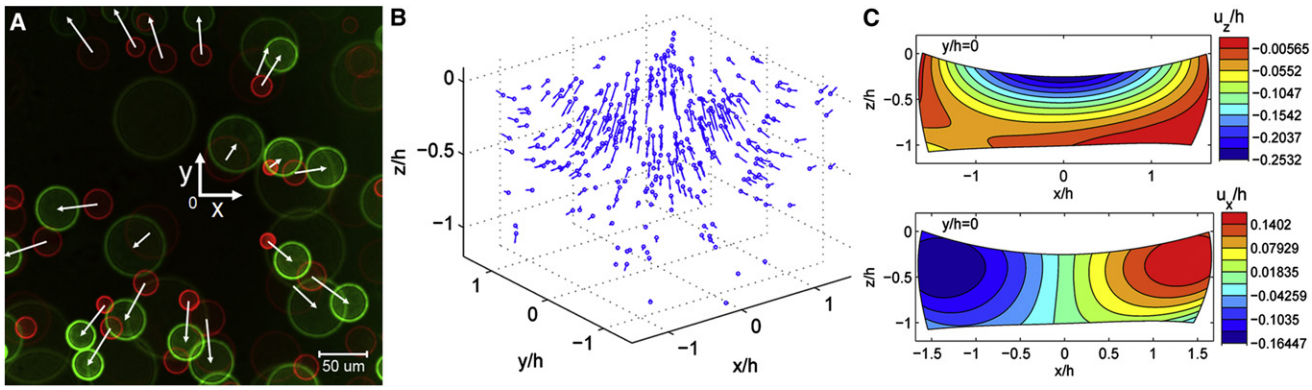

FIGURE 3 Displacement field in the indented gel. (*A*) Combined images of fluorescent beads embedded in the un-deformed and deformed polyacrylamide gel. The red defocused rings indicate the original bead position in un-deformed gel; (*green rings*) positions of fluorescent beads within the deformed gel. (*White arrows*) The xy displacement of each bead in x-y plane upon indentation. Increase in ring size indicates displacement in the negative z direction. (*B*) Experimentally measured three-dimensional bead displacements. The lengths of the arrows are scaled by a factor of 0.7 for better illustration. (*Circles*) Initial position of beads; (*ends* of the *arrows*) final positions of the beads after the gel is indented. (*C*) Continuous displacement field of u_z/h and u_x/h at cross section $y = 0$ (*side view*). The displacement fields are derived from the discrete displacements shown in panel *B* using MLSIM.

used as the (0,0,0) coordinates for all the measurements. The combined bead displacements were shown in Fig. 3 *B*.

Moving least-square method

The bead-displacement data obtained from defocused particle-tracking provides a discrete measurement of displacement fields within the soft gel. Because the strains are spatial derivatives of displacements, evaluating them requires a continuous description of the displacement fields. The basic idea here is to construct a continuously differentiable displacement field from these discrete data using interpolation. Our interpolation scheme draws an idea from the mesh-free method (26) in computational mechanics, developed as an alternative to the finite-element method. This method uses the moving least-square (MLS) interpolation technique (30–32). An advantage of the MLS method is that the interpolated field can have a continuous derivative of any order, thus ensuring a smooth strain field. Following Belytschko et al. (26), we first construct an interpolation function $g(\mathbf{x})$ as

$$g(\mathbf{x}) = \mathbf{P}^T(\mathbf{x})\mathbf{a}(\mathbf{x}), \tag{1}$$

where $\mathbf{x}$ represents the Cartesian coordinates (x,y,z) of a point in the undeformed configuration ($\mathbf{x}^T = [x, y, z]$; the superscript T denotes transpose). $\mathbf{P}^T(\mathbf{x})$ is a polynomial basis and $\mathbf{a}(\mathbf{x}) = [a_0(\mathbf{x}),a_1(\mathbf{x}),a_2(\mathbf{x}), \ldots]^T$ can be regarded as unknown coefficients for this basis. Note that $a_i(\mathbf{x})$ values are scalar functions of position. For example, if a linear basis is used, $\mathbf{P}^T(\mathbf{x})$ and $g(\mathbf{x})$ are

$$\mathbf{P}^T(\mathbf{x}) = [1, x, y, z], \tag{2a}$$

$$g(\mathbf{x}) = a_0(\mathbf{x}) + a_1(\mathbf{x})x + a_2(\mathbf{x})y + a_3(\mathbf{x})z. \tag{2b}$$

We adopt a cubic basis in our data processing, i.e.,

$$\mathbf{P}^T(\mathbf{x}) = \begin{bmatrix}1, x, y, z, x^2, y^2, z^2, xy, xz, yz, x^3, y^3, z^3, \ldots \\ x^2y, x^2z, y^2x, y^2z, z^2x, z^2y, xyz\end{bmatrix}. \tag{2c}$$

It is important to note that $\mathbf{a}(\mathbf{x})$ depends on $\mathbf{x}$, otherwise $g(\mathbf{x})$ reduces to a regular polynomial function. Suppose in the undeformed gel there are n beads located at $\mathbf{b}_I$ ($I = 1,\ldots,n$), where $\mathbf{b}_I^T = [b_{Ix},b_{Iy},b_{Iz}]$. Let w_I denote a physical quantity associated with bead I (e.g., the x component of the displacement of the I^{th} bead). To determine the coefficient functions $\mathbf{a}(\mathbf{x})$, we perform a weighted least-square fitting at every point $\mathbf{x}$ that minimizes the following norm,

$$L = \sum_{I=1}^{n} f(\boldsymbol{x} - \boldsymbol{b}_I)\left[\boldsymbol{P}^T(\boldsymbol{b}_I)\boldsymbol{a}(\boldsymbol{b}_I) - w_I\right]^2, \tag{3}$$

where $f(\boldsymbol{x} - \boldsymbol{b}_I)$ is a weight function that decays with $|\boldsymbol{x} - \boldsymbol{b}_I|$, that is, the weight decreases as the point of interest moves away from bead I. As a result, the coefficients $\mathbf{a}(\mathbf{x})$ varies from point to point and is determined mostly by the displacements of beads within a neighborhood of $\mathbf{x}$. We used the following exponentially decaying weight function proposed by Belytschko et al. (26),

$$f(\mathbf{x} - \mathbf{b}_I) = \begin{cases} \dfrac{\exp\left(1 - d^2/d_m^2\right) - 1}{e - 1} & d \le d_m \\ 0 & d > d_m \end{cases}, \quad d = |\mathbf{x} - \mathbf{b}_I|. \tag{4}$$

In Eq. 4, d_m is a cut-off distance and is chosen to be

$$d_m = 2\sum_{I=1}^{m}\frac{|\mathbf{x} - \mathbf{b}_I|}{m}, \tag{5}$$

where m is an adjustable parameter that is smaller than n, the total bead number. This parameter determines the decaying length of the weight function f and thus controls the quality of the fitted results. For example, if m is too small, only a few bead-data points are included in the MLS fitting, which can cause severe nonsmoothness in the fitted fields. As m increases toward the total bead number n, the fitted field becomes smoother but should converge at a large enough m. This is because the newly added data points, arrived upon by further increasing m, contribute little to the MLS fitting due to the exponential decaying behavior of the weight function. We have verified in our indentation data that the fitted strain fields are insensitive to m for $m = 180$ and $m = 285$ (total bead number is 285). We chose $m = 180$ to save computation time while achieving sufficient accuracy.

To determine the unknown vector function $\mathbf{a}(\mathbf{x})$, we minimize the least-square error norm L in Eq. 3. This procedure leads to a set of linear equations for the vector function $\mathbf{a}(\mathbf{x})$, which can be solved exactly. The interpolation function is found to be

$$g(\mathbf{x}) = \mathbf{P}^T(\mathbf{x})\mathbf{a}(\mathbf{x}) = \mathbf{P}^T(\mathbf{x})\mathbf{A}^{-1}(\mathbf{x})\mathbf{B}(\mathbf{x})\mathbf{w}, \tag{6}$$

where

$$\mathbf{A}(\mathbf{x}) = \sum_{I=1}^{n} f(\mathbf{x} - \mathbf{b}_I)\mathbf{P}(\mathbf{b}_I)\mathbf{P}^T(\mathbf{b}_I), \tag{7a}$$

$$\mathbf{B}(\mathbf{x}) = [f(\mathbf{x} - \mathbf{b}_1)\mathbf{P}(\mathbf{b}_1), \ldots, f(\mathbf{x} - \mathbf{b}_n)\mathbf{P}(\mathbf{b}_n)], \tag{7b}$$

$$\mathbf{w}^T = [w_1, w_2, \ldots, w_n]. \tag{7c}$$

Applying the interpolation function in Eq. 6 to each of the three displacement components, we obtain a continuously differentiable three-dimensional displacement field within the gel.

Computing strain and stress fields

The strain fields can be determined by calculating the spatial derivatives of the displacements. For simplicity, we use linear elasticity formulation where the strain tensor is given by

$$\begin{aligned} \varepsilon &= \frac{\left(\nabla\mathbf{u} + (\nabla\mathbf{u})^T\right)}{2}, \text{ or} \\ \varepsilon_{ij} &= \frac{1}{2}\left(\frac{\partial u_i}{\partial x_j} + \frac{\partial u_j}{\partial x_i}\right), \end{aligned} \tag{8}$$

where $\mathbf{u}$ is the displacement vector: $\mathbf{u}^T = [u_x, u_y, u_z]$. The subscripts i and j can be 1, 2, or 3, referring to the Cartesian coordinates x, y, and z, respectively. Equation 8 allows us to compute the strain from the interpolated displacement field using the derivatives of the interpolation function:

$$\frac{\partial g}{\partial x_i} = \left[\frac{\partial \mathbf{P}^T}{\partial x_i}\mathbf{A}^{-1}\mathbf{B} - \mathbf{P}^T\mathbf{A}^{-1}\frac{\partial \mathbf{A}}{\partial x_i}\mathbf{A}^{-1}\mathbf{B} + \mathbf{P}^T\mathbf{A}^{-1}\frac{\partial \mathbf{B}}{\partial x_i}\right]\mathbf{w}. \tag{9}$$

Once the strain field is determined, we can use the constitutive relations to obtain the stress field. Assuming the material is isotropic and homogeneous, the stress field is given by the Hooke's law in linear elasticity, i.e.,

$$\begin{aligned} \sigma_{ij} &= \lambda\varepsilon_b\delta_{ij} + 2\mu\varepsilon_{ij}, \\ \lambda &= \frac{2\nu\mu}{(1 - 2\nu)}, \end{aligned} \tag{10}$$

where $\varepsilon_b = \varepsilon_{xx} + \varepsilon_{yy} + \varepsilon_{zz}$ is the bulk strain, μ is the shear modulus, and ν is the Poisson's ratio.

A difficulty arises when the gel is incompressible or close to incompressible, that is, when $\nu \sim 0.5$ (or $\lambda \to \infty$). In this case, the bulk strain ε_b is close

to zero so it is very difficult to numerically evaluate the product $\lambda\varepsilon_b$. As a result, the normal stress components (e.g., σ_{zz}) cannot be directly determined from the strain field. Because the short-time mechanical behavior of most gels is close to incompressible, the determination of the full stress tensor from the strains is a nontrivial problem that needs to be addressed. For an incompressible material, $\lambda\varepsilon_b$ is the average of the three normal stress components and is usually denoted by $-p$, where p is often interpreted as a hydrostatic pressure (33). It should be noted that the $\lambda\varepsilon_b$ term in Eq. 10 is taken to be zero for incompressible materials in previous works (20,23). Because an incompressible material can support hydrostatic stress without deformation, the assumption of $\lambda\varepsilon_b = 0$ may lead to substantial error in the calculation of stresses in the gel. To illustrate this point, we consider a simple example where a concentrated compressive normal force acts on the surface of an incompressible linear elastic half-space. An exact solution for the stress field, known as the Boussinesq solution, has been obtained and can be found in Johnson (34). Using this solution, one can easily show that setting $\lambda\varepsilon_b = 0$ in Eq. 10 makes at least 33% relative error for all three normal stress components.

We propose the following solution to resolve this problem. As mentioned earlier, for incompressible solids, the $\lambda\varepsilon_b$ term in Eq. 10 should be replaced by an undetermined pressure term $-p$ (33), i.e.,

$$\sigma_{ij} = -p\delta_{ij} + 2\mu\varepsilon_{ij}, \tag{11}$$

where δ_{ij} is the Krönecker delta defined by $\delta_{ij} = 0$ if $i \neq j$ and $\delta_{ij} = 1$ otherwise. The stresses must satisfy the following equilibrium equations under static or quasistatic conditions:

$$\sum_{j=1}^{3} \frac{\partial \sigma_{ij}}{\partial x_j} = 0. \tag{12}$$

Substituting Eq. 11 into Eq. 12, we obtain

$$\frac{\partial p}{\partial x_i} = \mu\nabla^2 u_i + \mu\frac{\partial \varepsilon_b}{\partial x_i}. \tag{13}$$

Integrating Eq. 13 gives

$$p(\mathbf{x}) - p(\mathbf{x}_0) = \mu \int_{\mathbf{x}_0}^{\mathbf{x}} \left(\nabla^2\mathbf{u}\right)\cdot d\mathbf{s} + \mu[\varepsilon_b(\mathbf{x}) - \varepsilon_b(\mathbf{x}_0)]. \tag{14}$$

The first integral in Eq. 14 can be evaluated along any path joining $\mathbf{x}_0$ to $\mathbf{x}$. Usually one can choose $\mathbf{x}_0$ so that $p(\mathbf{x}_0)$ is known, e.g., $\mathbf{x}_0$ can be a point where all the stress components vanish (e.g., far away from our region of interest) or a point where one of the normal stress components is known. In principle, $\varepsilon_b = 0$ is valid for incompressible materials at any spatial locations; we retain the bulk strain term in Eq. 13, because it may not be exactly zero in experiments. For compressible solids, the equations above are also valid but may not be very useful in this case because the stresses can be directly determined from strains. The term $\nabla^2\mathbf{u}$ in Eq. 14 is obtained by taking the Laplacian of the interpolation function in Eq. 6, which is found to be

$$\begin{aligned}\nabla^2 g = \Big[&\left(\nabla^2\mathbf{P}^T\right)\mathbf{A}^{-1}\mathbf{B} - \mathbf{P}^T\mathbf{A}^{-1}\left(\nabla^2\mathbf{A}\right)\mathbf{A}^{-1}\mathbf{B} + \mathbf{P}^T\mathbf{A}^{-1}\left(\nabla^2\mathbf{B}\right) \\ &+ \sum_{i=1}^{3} 2\frac{\partial \mathbf{P}^T}{\partial x_i}\left(-\mathbf{A}^{-1}\frac{\partial \mathbf{A}}{\partial x_i}\mathbf{A}^{-1}\mathbf{B} + \mathbf{A}^{-1}\frac{\partial \mathbf{B}}{\partial x_i}\right) \\ &+ \sum_{i=1}^{3} 2\mathbf{P}^T\left(\mathbf{A}^{-1}\frac{\partial \mathbf{A}}{\partial x_i}\mathbf{A}^{-1}\frac{\partial \mathbf{A}}{\partial x_i}\mathbf{A}^{-1}\mathbf{B}\right. \\ &\left.- \mathbf{A}^{-1}\frac{\partial \mathbf{A}}{\partial x_i}\mathbf{A}^{-1}\frac{\partial \mathbf{B}}{\partial x_i}\right)\Big]\mathbf{w}. \end{aligned} \tag{15}$$

The pressure field is determined by Eq. 14, where we evaluate $\nabla^2\mathbf{u}$ by applying Eq. 15 to each of the three displacement components u_i. Once the pressure field is obtained, the stress field can be easily calculated using Eq. 11.

Finite-element analysis

In our early work and others, it has been found that the gel deformation depends sensitively on gel thickness h (28,29). More specifically, the gel deformation is found to depend on two parameters, R/h and δ/h, where R is the radius of the indenter and δ is the indentation depth at the contact point (see text and the Supporting Material of Long et al. (29)). We thus chose values of $R/h = 4.366$ and $\delta/h = 0.2532$ to be exactly the same as in experiments for the finite-element method (FEM) calculation. Note that, in experiments, we have ball radius $R = 585$ μm, the gel layer thickness $h = 134$ μm, and the indentation depth $\delta = 33.93$ μm. Briefly, the deformation of the gel layer is simulated using the commercial finite-element software ABAQUS (Ver. 6.7; Dassault Systèmes, Providence, RI).

Axisymmetry of the indentation setup allows us to use axisymmetric elements to simulate gel deformation. The gel layer was modeled as a circular disk with thickness h and radius $20h$ made of incompressible neo-Hookean solid, which is the simplest hyperelastic material model for elastomers and was derived based on the Gaussian statistics of polymer chains (35). The indenter was modeled as a rigid sphere of radius R and the indenter-gel interface was assumed to be in frictionless condition. The gel layer was discretized into 25,547 linear quadrilateral axisymmetric elements (CAX4RH) biased toward the center of contact region, where the element size is ~$0.0167h$. Hybrid elements were used where the hydrostatic pressure field due to incompressibility was independently interpolated and was solved together with the displacement field through the finite-element equations.

RESULTS AND DISCUSSIONS

Discrete and continuous displacement fields in the gel

The discrete displacements of the embedded fluorescent beads upon the deformation of the gel were obtained using the three-dimensional defocused particle-tracking method. A three-dimensional plot of the bead positions and bead displacements is shown in Fig. 3 *B*. A total of 285 fluorescent beads were tracked in this data set. Depending on the location of a bead, magnitudes of the measured bead displacement ranges from 0.5 μm to 35 μm, demonstrating the highly nonuniform deformation field within the gel.

We first computed the continuous and differentiable displacement field using the discrete bead displacements, which was a necessary step for computing the three-dimensional strain field. Using the MLSIM introduced above, we transformed the discrete bead displacements shown in Fig. 3 *B* into a continuous displacement field (Fig. 3 *C*). The characteristic deformation field due to an indenter is distinctly shown in Fig. 3 *C*. For clear presentation, we took advantage of axisymmetry of the deformation field and choose to render the displacement field on the cross section of $y = 0$. The contours of displacement components u_x and u_z at the cross section of $y = 0$ are shown in Fig. 3 *C*. The displacement component u_y is negligible in this plane,

as expected from the axisymmetry of the deformation field. Fig. 3 *C* shows that the absolute values of u_x and u_z are symmetric with respect to the $x = 0$ plane. Therefore, in the following discussion we only present results in the plane $y = 0$ and $x > 0$ as shown in Fig. 4.

Experimentally obtained three-dimensional strain field

We compute the strain fields using Eqs. 8 and 9 from the continuously differentiable displacement field shown in Fig. 3 *C* or Fig. 4 (*A* and *C*). The results are plotted in Fig. 5 for the three normal strain components: ε_{xx}, ε_{yy}, ε_{zz}. Because of the axisymmetry, ε_{xz} is the only nonvanishing shear strain component on the $y = 0$ plane out of the three: ε_{xy}, ε_{yz}, ε_{xz}. Equation 10 indicates that ε_{xz} is proportional to the shear stress σ_{xz} by a coefficient of 2μ. As a result, the ε_{xz} component is not included in Fig. 5 because it has a similar distribution to σ_{xz}, which will be presented in Fig. 6.

As mentioned earlier, at a timescale much shorter than the characteristic diffusion time, gels behave as incompressible materials due to negligible amount of solvent migration. This is the case for our indentation experiment, because the experimental timescale is approximately several minutes and the diffusion timescale is on the order of hours (29). Therefore, we set the Poisson's ratio for the polyacrylamide gel in our experiment to be 0.5, which is consistent with the compression test result in Maskarinec et al. (20) where the Poisson's ratio of polyacrylamide gels was measured to be 0.48–0.5. To further verify the incompressibility, we evaluate the determinant of the deformation gradient det(**F**) using our bead data. Note that $F_{ij} = \delta_{ij} + \partial u_i/\partial x_j$. Its determinant det(**F**) equals to the ratio of the deformed volume of a material element versus its undeformed volume. It turned out that det(**F**) ranges from 0.93 to 1.07 in most region, suggesting that the local volume change was within $\pm 7\%$. Given that the magnitude of strains can be up to 30% (see Fig. 5), such a small local volume change confirms that the gel has a Poisson's ratio close to 0.5.

Experimentally obtained three-dimensional stress field

Because the gel is nearly incompressible, directly calculating the stress fields using Eq. 10 with a Poisson's ratio close to 0.5 can induce significant numerical errors. In this case, we need to compute the pressure and stress fields using Eqs. 11, 14, and 15. Recall that to determine the pressure field $p(\mathbf{x})$, Eq. 14 requires a reference point $\mathbf{x}_0$ where the pressure is known. Ideally the reference point should be very far away from the deformation region such that all stress components vanish at this point. However, this is

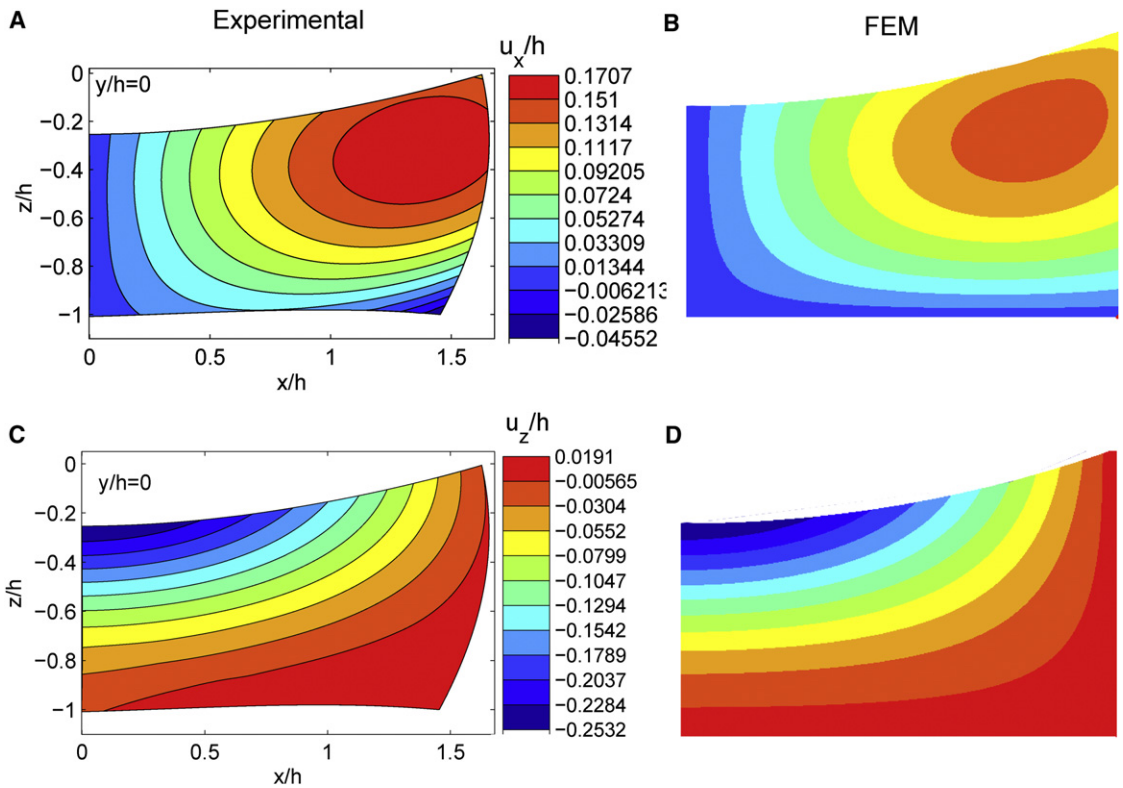

FIGURE 4 Continuous displacement fields from experiments and FEM calculations. Contour plots of the continuous displacement field u_x/h (*A* and *B*) and u_z/h (*C* and *D*) at the cross section $y = 0$ and $x > 0$. The same color map is used for experiments and FEM calculations.

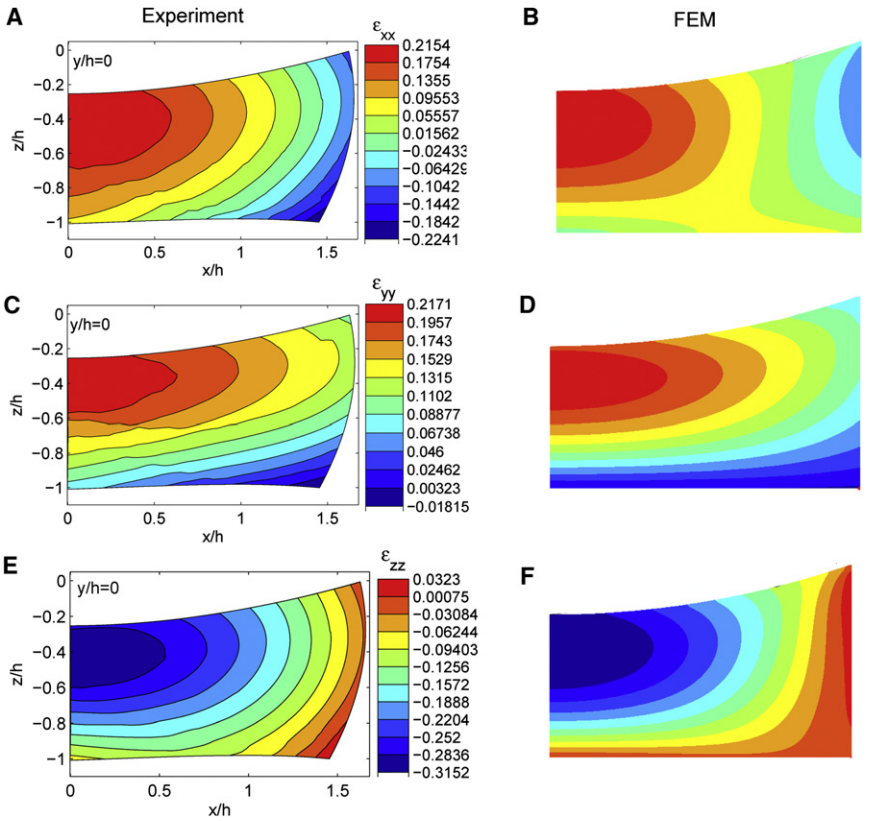

FIGURE 5 Strain fields from experiments and FEM calculations. Contour plots of strain field ε_{xx} (*A* and *B*), ε_{yy} (*C* and *D*), and ε_{zz} (*E* and *F*) at the cross section $y = 0$ and $x > 0$. The same color map is used for experiments and FEM calculations.

limited by the finite imaging volume of our experimental data, outside which there is no data points acquired for bead displacements. Therefore, we would not be able to compute the pressure field according to Eq. 14 if the reference point were chosen outside the imaging volume. Here we choose the reference point to be on the top surface of the gel layer ($z = 0$) and as far away from the contact center as possible. Specifically, the reference point is chosen to be $x_0 = 1.5h$, $y_0 = 0$, and $z_0 = 0$. At this point, the normal stress σ_{zz} should be zero because the surface is traction-free. This condition, together with Eq. 13, implies that $p(\mathbf{x}_0) = 2\mu\varepsilon_{zz}(\mathbf{x}_0)$. This result and the value of $\varepsilon_{zz}(\mathbf{x}_0)$ from the obtained strain field allow us to compute the pressure field using Eq. 14 and then determine the stress field using Eq. 13. The experimentally determined stress field is shown in Fig. 6 for two normal stress components: σ_{xx}, σ_{zz}, and a shear stress component σ_{xz}. Fig. 6, *A* and *C*, suggests that the normal stresses are concentrated around the center of the contact region as expected, because this is the most severely deformed region within the gel.

Note that the stresses plotted in Fig. 6 were normalized by the Young's modulus E, which can indeed be measured from our indentation data. Because the indenting force is 12.4 μN, gel layer thickness is h =134 μm, indenter radius is R =585 μm (see Indentation Method), and indentation depth is δ =33.93 μm (see Finite-element analysis), taking the Poisson's ratio to be 0.5, the Young's modulus E is calculated to be 283 Pa using the formula in Long et al. (29), and the shear modulus μ is 94 Pa.

Validation of the experimentally obtained three-dimensional strain and stress field using finite-element analysis

To validate the described three-dimensional full-field strain and stress mapping technique, we carried out an independent finite-element analysis to determine the displacement, stress, and strain fields within a thin polyacrylamide gel using the same setup as in our indentation experiments (see Fig. 1). The experimentally determined displacement fields (Fig. 4, *A* and *C*) agree well with the FEM results (Fig. 4, *B* and *D*). Note that the contour levels in the experimental determined displacement fields were set to be the same as the FEM results, except for the maximum and minimum limits. Furthermore, the experimentally acquired strain fields (Fig. 5, *A*, *C*, and *E*) agree well with those from FEM calculations (Fig. 5, *B*, *D*, and *F*). This demonstrates the validity of the displacement measurements and the MLS interpolation method.

The stress fields σ_{xx}, σ_{zz}, and σ_{xz} from experiments are plotted and compared with FEM results both in contour plots and numerical plot (Fig. 6, *A*–*G*). Although the experimental results underestimate the magnitude of the normal stress components compared with FEM data, the distribution

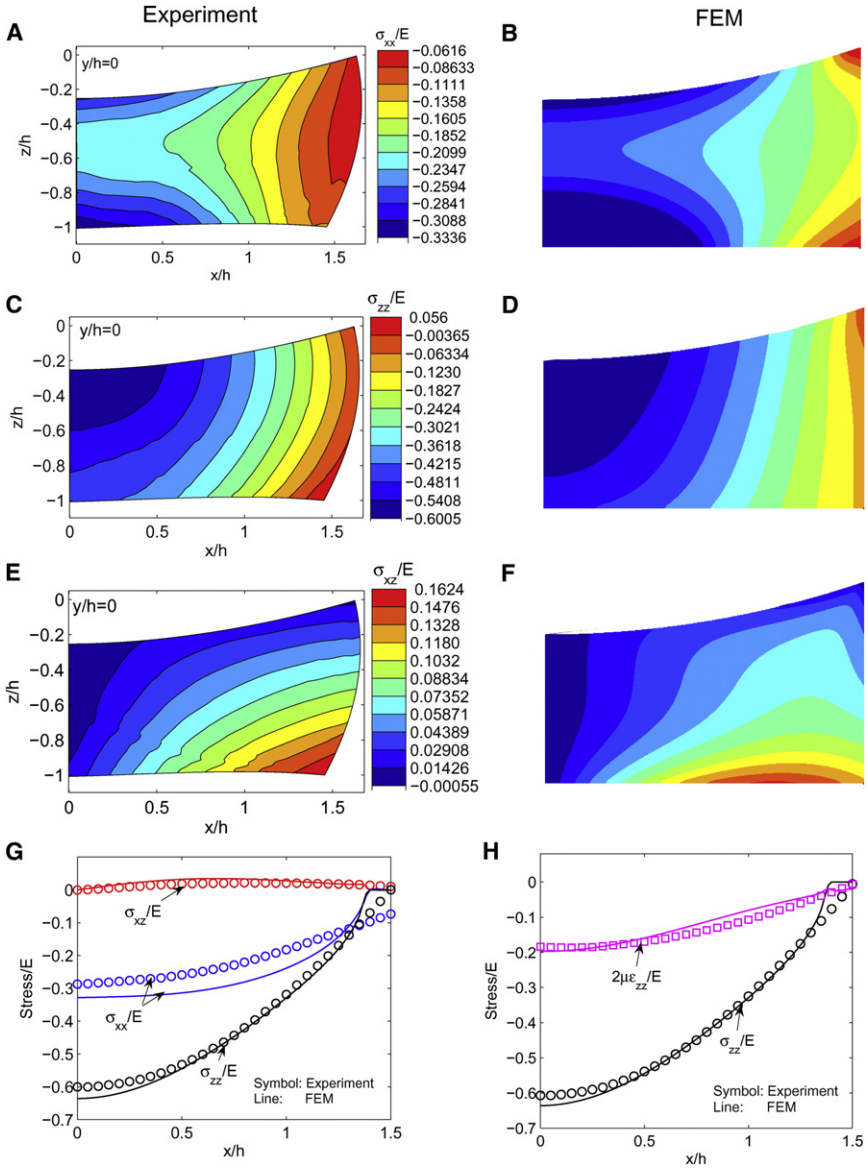

FIGURE 6 Stress field from experiments and FEM calculations. Contour plots of stress-field σ_{xx}/E (*A* and *B*) σ_{zz}/E (*C* and *D*), and σ_{xz}/E (*E* and *F*) at the cross section $y = 0$ and $x > 0$. The same color map is used for experiments and FEM calculations. (*G*) The normalized stresses versus x at the contact interface ($y = 0$ and $z = 0$). (*Symbols*) Experimental results; (*lines*) FEM results. (*H*) The normalized normal stress σ_{zz}/E, and $2\mu\varepsilon_{zz}/E$ at the contact interface ($y = 0$ and $z = 0$). (*Symbols*) Experimental results; (*lines*) FEM results.

of stresses are still very well captured. Fig. 6 *G* plots the normalized stresses as functions of x/h on the contacting interface ($z = 0$, $y = 0$), further verifying our experimental techniques.

To highlight the importance of the hydrostatic pressure field, we plot the stress component σ_{zz} as well as $2\mu\varepsilon_{zz}$ (both normalized by E) on the contacting interface in Fig. 6 *H*. Note that if the pressure term (or the $\lambda\varepsilon_b$ term in Eq. 10) were set to zero, the normal stress σ_{zz} would be equal to $2\mu\varepsilon_{zz}$. Fig. 6 *H* clearly showed the significant deviation of $2\mu\varepsilon_{zz}$ from the stress σ_{zz} obtained from experimental or FEM results, thus demonstrating the necessity of accurately evaluating the pressure field. Furthermore, the excellent agreement between experimentally determined σ_{zz} and the FEM results validates our method of computing the pressure field.

CONCLUSIONS AND FUTURE PERSPECTIVES

In summary, we have developed a three-dimensional full-field material characterization method for mapping the strain and stress field within a soft and transparent gel using a fluorescence microscope and a forward-computation algorithm. This technique, together with an apparently new method to compute the stress field in an incompressible elastic solid, allows us to map the strain and stress fields within a thin polyacrylamide gel when deformed by the weight of a millimeter-scale glass sphere. The measured strain and stress fields agree well with those obtained from the finite-element method.

The use of the three-dimensional defocused particle imaging method enables us to optimize the spatial and temporal resolutions needed for each application. Table 1

TABLE 1 Spatial and temporal resolutions of the three-dimensional traction microscopy

Optimize for:	Spatial resolution	Temporal resolution	Image volume
Magnification	40× (0.6 NA)	40× (0.6 NA)	20× (0.4 NA)
Number of images	10	1	10
Total image volume (μm^3)	205 × 205 × 150	205 × 205 × 40	410 × 410 × 300
Bead-to-bead spacing (μm)	20	30	40
Acquisition time (s)	10	0.1	10
Single bead position accuracy (μm)	0.2 × 0.2 × 0.4	0.2 × 02 × 0.4	0.4 × 0.4 × 0.8

lists the spatial and temporal resolutions for the imaging system that we have (microscope: IX 51, Olympus America, Center Valley, PA; camera: DALSA 512B, EM, Waterloo, CA). For instance, to optimize the temporal resolution, we will take a single image for bead position measurements at a frame rate of 10 fps. Under this scenario, the temporal resolution is 0.1 s and the fluorescent-bead concentration expressed as average bead-to-bead spacing is 30 μm for a 40× objective. To obtain a larger imaging volume, one can use a smaller magnification objective lens. In this case, a 20× objective lens will be able to increase the imaging volume by eight times in comparison to a 40× lens. In addition, we can also take multiple images (10 in Table 1) along the z direction using an automatic z-translation stage to increase the imaging volume.

The main challenge is to reduce the spatial resolution for the bead-displacement measurements. As of this writing, the average bead-to-bead spacing is 20–30 μm (see Table 1) for the three-dimensional defocused particle-tracking method to work effectively. This limitation is imposed by the ability to track overlapping rings when the beads are too close together. This problem can be resolved by 1), embedding fluorescent beads of different colors; and 2), improving the tracking software. By embedding fluorescent beads of four different colors, one can reach a bead-to-bead spacing resolution of 12.5 μm. The current tracking software only takes into account the information of the ring diameter; however, the light intensity around the ring can also be used to identify the bead position.

Looking forward, the presented technique can be readily adapted to map the strain and stress field around a living cell embedded in a three-dimensional ECM. The fast temporal resolution will allow us to probe cell traction force of cell types that change mechanically at a timescale that a confocal cannot handle (for example, cardiomyocytes). The use of a fluorescence microscope allows this technique to be more accessible to biology labs, in comparison to the current three-dimensional traction microscopy where confocal microscopy is required. The introduction of a moving least-squared method generates a straightforward, easy-to-implement method for mapping the three-dimensional strain field in a soft gel using discrete bead displacements. More importantly, the forward computation algorithm (in comparison to solving an inverse problem using Green's function (22)) does not require that the biomaterials be linear or that the deformation be small. Many commonly-used natively-derived biomaterials, such as collagen and fibrin, are known to exhibit nonlinear elastic behavior (27). To extend the presented technique to nonlinear biological materials, one needs to simply modify the relation of stress and strain field using a nonlinear elasticity theory. This work is in progress as of this writing, and will be presented in a future publication.

M.S.H. and M.W. thank Joseph Califano and Cynthia Reinhart-King for their help with the polyacrylamide gel preparation and the microsphere indentation method, and Yu Li Wang for insightful discussions.

M.S.H., R.L., and M.W. acknowledge support from the National Center for Research Resources (grant No. 5R21RR025801-03) and the National Institute of General Medical Sciences (grant No. 8 R21 GM103388-03) of the National Institutes of Health. R.L. acknowledges support from the Materials and Surface Engineering program, Capability Maturity Model Integration, National Science Foundation (grant no. CMMI-0900586). C.-Y.H. acknowledges the support of the US Department of Energy, Office of Basic Energy Science, Division of Material Sciences and Engineering, under award No. DE-FG02-07ER46463.

REFERENCES

1. Discher, D. E., P. Janmey, and Y. L. Wang. 2005. Tissue cells feel and respond to the stiffness of their substrate. *Science.* 310:1139–1143.
2. Chen, C. S. 2008. Mechanotransduction—a field pulling together? *J. Cell Sci.* 121:3285–3292.
3. Ulrich, T. A., E. M. de Juan Pardo, and S. Kumar. 2009. The mechanical rigidity of the extracellular matrix regulates the structure, motility, and proliferation of glioma cells. *Cancer Res.* 69:4167–4174.
4. Engler, A. J., S. Sen, …, D. E. Discher. 2006. Matrix elasticity directs stem cell lineage specification. *Cell.* 126:677–689.
5. Isenberg, B. C., P. A. Dimilla, …, J. Y. Wong. 2009. Vascular smooth muscle cell durotaxis depends on substrate stiffness gradient strength. *Biophys. J.* 97:1313–1322.
6. Pelham, Jr., R. J., and Y. Wang. 1997. Cell locomotion and focal adhesions are regulated by substrate flexibility. *Proc. Natl. Acad. Sci. USA.* 94:13661–13665.
7. Peyton, S. R., and A. J. Putnam. 2005. Extracellular matrix rigidity governs smooth muscle cell motility in a biphasic fashion. *J. Cell. Physiol.* 204:198–209.
8. Tee, S.-Y., J. Fu, …, P. A. Janmey. 2011. Cell shape and substrate rigidity both regulate cell stiffness. *Biophys. J.* 100:L25–L27.
9. Engler, A., L. Bacakova, …, D. Discher. 2004. Substrate compliance versus ligand density in cell on gel responses. *Biophys. J.* 86:617–628.
10. Griffith, L. G., and M. A. Swartz. 2006. Capturing complex 3D tissue physiology in vitro. *Nat. Rev. Mol. Cell Biol.* 7:211–224.
11. Hebner, C., V. M. Weaver, and J. Debnath. 2008. Modeling morphogenesis and oncogenesis in three-dimensional breast epithelial cultures. *Annu. Rev. Pathol.* 3:313–339.
12. Weaver, V. M., O. W. Petersen, …, M. J. Bissell. 1997. Reversion of the malignant phenotype of human breast cells in three-dimensional

culture and in vivo by integrin blocking antibodies. *J. Cell Biol.* 137:231–245.

13. Levental, K. R., H. Yu, …, V. M. Weaver. 2009. Matrix crosslinking forces tumor progression by enhancing integrin signaling. *Cell.* 139:891–906.
14. Cukierman, E., R. Pankov, …, K. M. Yamada. 2001. Taking cell-matrix adhesions to the third dimension. *Science.* 294:1708–1712.
15. Haessler, U., M. Pisano, …, M. A. Swartz. 2011. Dendritic cell chemotaxis in 3D under defined chemokine gradients reveals differential response to ligands CCL21 and CCL19. *Proc. Natl. Acad. Sci. USA.* 108:5614–5619.
16. Wolf, K., S. Alexander, …, P. Friedl. 2009. Collagen-based cell migration models in vitro and in vivo. *Semin. Cell Dev. Biol.* 20: 931–941.
17. Dembo, M., and Y. L. Wang. 1999. Stresses at the cell-to-substrate interface during locomotion of fibroblasts. *Biophys. J.* 76:2307–2316.
18. Frey, M. T., A. Engler, …, Y. L. Wang. 2007. Microscopic methods for measuring the elasticity of gel substrates for cell culture: microspheres, microindenters, and atomic force microscopy. *Methods Cell Biol.* 83:47–65.
19. Schwarz, U. S., N. Q. Balaban, …, S. A. Safran. 2002. Calculation of forces at focal adhesions from elastic substrate data: the effect of localized force and the need for regularization. *Biophys. J.* 83:1380–1394.
20. Maskarinec, S. A., C. Franck, …, G. Ravichandran. 2009. Quantifying cellular traction forces in three dimensions. *Proc. Natl. Acad. Sci. USA.* 106:22108–22113.
21. Hur, S. S., Y. Zhao, …, S. Chien. 2009. Live cells exert three-dimensional traction forces on their substrata. *Cell. Mol. Bioeng.* 2:425–436.
22. Legant, W. R., J. S. Miller, …, C. S. Chen. 2010. Measurement of mechanical tractions exerted by cells in three-dimensional matrices. *Nat. Methods.* 7:969–971.
23. Franck, C., S. A. Maskarinec, …, G. Ravichandran. 2011. Three-dimensional traction force microscopy: a new tool for quantifying cell-matrix interactions. *PLoS ONE.* 6:e17833.
24. Ramachandran, G. 2007. Three-dimensional full-field measurements of large deformations in soft materials using confocal microscopy and digital volume correlation. *Exp. Mech.* 47:427–438.
25. Wu, M., J. W. Roberts, and M. Buckley. 2005. Three-dimensional fluorescent particle tracking at micron-scale using a single camera. *Exp. Fluids.* 38:461–465.
26. Belytschko, T., Y. Y. Lu, and L. Gu. 1994. Element-free Galerkin methods. *Int. J. Numer. Methods Eng.* 37:229–256.
27. Storm, C., J. J. Pastore, …, P. A. Janmey. 2005. Nonlinear elasticity in biological gels. *Nature.* 435:191–194.
28. Reinhart-King, C. A., M. Dembo, and D. A. Hammer. 2003. Endothelial cell traction forces on RGD-derivatized polyacrylamide substrata. *Langmuir.* 19:1573–1579.
29. Long, R., M. S. Hall, …, C. Y. Hui. 2011. Effects of gel thickness on microscopic indentation measurements of gel modulus. *Biophys. J.* 101:643–650.
30. Lancaster, P., and K. Salkauskas. 1981. Surfaces generated by moving least-squares methods. *Math. Comput.* 37:141–158.
31. McLain, D. H. 1974. Drawing contours from arbitrary data points. *Comput. J.* 17:318–324.
32. Gordon, W. J., and J. A. Wixom. 1978. Shepards method of metric interpolation to bivariate and multivariate interpolation. *Math. Comput.* 32:253–264.
33. Landau, L. D., and E. M. Lifshitz. 1986. Theory of Elasticity, 3rd Ed. Butterworth-Heinemann, Oxford, UK.
34. Johnson, K. L. 1987. Contact Mechanics. Cambridge University Press, Cambridge, UK.
35. Treloar, L. R. G. 1946. The elasticity of a network of long-chain molecules. 3. *Trans. Faraday Soc.* 42:83–94.